Broadband near-field infrared spectromicroscopy using photothermal probes and synchrotron radiation

Paul M. Donaldson,[1,2] Chris S Kelley,[1] Mark D. Frogley,[1] Jacob Filik,[1] Katia Wehbe,[1] and Gianfelice Cinque[1,*]

[1]*Beamline B22 (MIRIAM), Diamond Light Source Ltd, Diamond House, Harwell Science & Innovation Campus, Didcot, Oxon, OX11 0DE, UK*
[2]*Central Laser Facility, Research Complex at Harwell, Harwell Science & Innovation Campus, Didcot, Oxon, OX11 0FA, UK*
[*]*gianfelice.cinque@diamond.ac.uk*

Abstract: In this paper, we experimentally demonstrate the use of infrared synchrotron radiation (IR-SR) as a broadband source for photothermal near-field infrared spectroscopy. We assess two methods of signal transduction; cantilever resonant thermal expansion and scanning thermal microscopy. By means of rapid mechanical chopping (50-150 kHz), we modulate the IR-SR at rates matching the contact resonance frequencies of atomic force microscope (AFM) cantilevers, allowing us to record interferograms yielding Fourier transform infrared (FT-IR) photothermal absorption spectra of polystyrene and cyanoacrylate films. Complementary offline measurements using a mechanically chopped CW IR laser confirmed that the resonant thermal expansion IR-SR measurements were below the diffraction limit, with a spatial resolution better than 500 nm achieved at a wavelength of 6 μm, i.e. λ/12 for the samples studied. Despite achieving the highest signal to noise so far for a scanning thermal microscopy measurement under conditions approaching near-field (dictated by thermal diffusion), the IR-SR resonant photothermal expansion FT-IR spectra measured were significantly higher in signal to noise in comparison with the scanning thermal data.

References and links

1. A. J. Sommer, "Mid-infrared Transmission Microspectroscopy," in *Handbook of Vibrational Spectroscopy*, J. M. Chalmers, and P. R. Griffiths, eds. (Wiley, 2001).
2. P. J. Treado and M. P. Nelson, "Raman Imaging," in *Handbook of Vibrational Spectroscopy*, J. M. Chalmers, and P. R. Griffiths, eds. (Wiley, 2001).
3. A. Marcelli and G. Cinque, "Chapter 3: infrared synchrotron radiation beamlines: high brilliance tools for IR spectromicroscopy," in *Biomedical Applications of Synchrotron Infrared Microspectroscopy: A Practical Approach* (The Royal Society of Chemistry, 2011), pp. 67–104.
4. X. G. Xu, M. Rang, I. M. Craig, and M. B. Raschke, "Pushing the sample-size limit of infrared vibrational nanospectroscopy: from monolayer toward single molecule sensitivity," J. Phys. Chem. Lett. **3**(13), 1836–1841 (2012).
5. F. Huth, A. Govyadinov, S. Amarie, W. Nuansing, F. Keilmann, and R. Hillenbrand, "Nano-FTIR absorption spectroscopy of molecular fingerprints at 20 nm spatial resolution," Nano Lett. **12**(8), 3973–3978 (2012).
6. A. D. Smith, M. R. F. Siggel-King, G. M. Holder, A. Cricenti, M. Luce, P. Harrison, D. S. Martin, M. Surman, T. Craig, S. D. Barrett, A. Wolski, D. J. Dunning, N. R. Thompson, Y. Saveliev, D. M. Pritchard, A. Varro, S. Chattopadhyay, and P. Weightman, "Near-field optical microscopy with an infra-red free electron laser applied to cancer diagnosis," Appl. Phys. Lett. **102**(5), 053701 (2013).
7. A. Dazzi, R. Prazeres, F. Glotin, and J. M. Ortega, "Local infrared microspectroscopy with subwavelength spatial resolution with an atomic force microscope tip used as a photothermal sensor," Opt. Lett. **30**(18), 2388–2390 (2005).

8. F. Lu and M. A. Belkin, "Infrared absorption nano-spectroscopy using sample photoexpansion induced by tunable quantum cascade lasers," Opt. Express **19**(21), 19942–19947 (2011).
9. C. Mayet, A. Dazzi, R. Prazeres, F. Allot, F. Glotin, and J. M. Ortega, "Sub-100 nm IR spectromicroscopy of living cells," Opt. Lett. **33**(14), 1611–1613 (2008).
10. C. Policar, J. B. Waern, M.-A. Plamont, S. Clède, C. Mayet, R. Prazeres, J.-M. Ortega, A. Vessières, and A. Dazzi, "Subcellular IR imaging of a metal-carbonyl moiety using photothermally induced resonance," Angew. Chem. Int. Ed. Engl. **50**(4), 860–864 (2011).
11. I. T. Lucas, A. S. McLeod, J. S. Syzdek, D. S. Middlemiss, C. P. Grey, D. N. Basov, and R. Kostecki, "IR near-field spectroscopy and imaging of single LixFePO4 microcrystals," Nano Lett. **15**(1), 1–7 (2015).
12. I. V. Pechenezhskiy, X. Hong, G. D. Nguyen, J. E. P. Dahl, R. M. K. Carlson, F. Wang, and M. F. Crommie, "Infrared spectroscopy of molecular submonolayers on surfaces by infrared scanning tunneling microscopy: tetramantane on Au111," Phys. Rev. Lett. **111**(12), 126101 (2013).
13. J. D' Archangel, E. Tucker, E. Kinzel, E. A. Muller, H. A. Bechtel, M. C. Martin, M. B. Raschke, and G. Boreman, "Near- and far-field spectroscopic imaging investigation of resonant square-loop infrared metasurfaces," Opt. Express **21**(14), 17150–17160 (2013).
14. P. Hermann, A. Hoehl, P. Patoka, F. Huth, E. Rühl, and G. Ulm, "Near-field imaging and nano-Fourier-transform infrared spectroscopy using broadband synchrotron radiation," Opt. Express **21**(3), 2913–2919 (2013).
15. H. A. Bechtel, E. A. Muller, R. L. Olmon, M. C. Martin, and M. B. Raschke, "Ultrabroadband infrared nanospectroscopic imaging," Proc. Natl. Acad. Sci. U.S.A. **111**(20), 7191–7196 (2014).
16. A. Centrone, "Infrared imaging and spectroscopy beyond the diffraction limit," Annu. Rev. Anal. Chem. **8**(1), 101–126 (2015).
17. L. Bozec, A. Hammiche, M. J. Tobin, J. M. Chalmers, N. J. Everall, and H. M. Pollock, "Near-field photothermal Fourier transform infrared spectroscopy using synchrotron radiation," Meas. Sci. Technol. **13**(8), 1217–1222 (2002).
18. A. Dazzi, F. Glotin, and R. Carminati, "Theory of infrared nanospectroscopy by photothermal induced resonance," J. Appl. Phys. **107**(12), 124519 (2010).
19. A. M. Katzenmeyer, G. Holland, K. Kjoller, and A. Centrone, "Absorption spectroscopy and imaging from the visible through mid-infrared with 20 nm resolution," Anal. Chem. **87**(6), 3154–3159 (2015).
20. A. Dazzi, C. B. Prater, Q. Hu, D. B. Chase, J. F. Rabolt, and C. Marcott, "AFM-IR: combining atomic force microscopy and infrared spectroscopy for nanoscale chemical characterization," Appl. Spectrosc. **66**(12), 1365–1384 (2012).
21. G. Cinque, M. Frogley, K. Wehbe, J. Filik, and J. Pijanka, "Multimode InfraRed Imaging and Microspectroscopy (MIRIAM) beamline at diamond," Synchrotron Radiat. News **24**(5), 24–33 (2011).
22. K. Wehbe, J. Filik, M. D. Frogley, and G. Cinque, "The effect of optical substrates on micro-FTIR analysis of single mammalian cells," Anal. Bioanal. Chem. **405**(4), 1311–1324 (2013).
23. G. P. Williams, "Filling the THz gap - high power sources and applications," Rep. Prog. Phys. **69**(2), 301–326 (2006).

1. Introduction

Vibrational spectromicroscopy is a powerful means of acquiring molecular absorption spectra as well as for imaging via a contrast mechanism that is rich in the chemical information. To this end, infrared (IR) and Raman spectromicroscopy are now widespread analytical tools with a complementary range of applications across a variety of disciplines, from biomedical analysis of single cells and histological tissue sections to materials science, cultural heritage and mineralogy, etc [1, 2].

Alongside light sources based on blackbody radiation and lasers, IR spectromicroscopy can significantly benefit from using IR synchrotron radiation (IR-SR) emitted from electron storage rings. IR-SR gives a unique combination of virtually unlimited spectral bandwidth (e.g. 1−2000 μm at MIRIAM beamline B22 of Diamond Light Source), far in excess of any laser, with high photon flux density per unit of solid angle. This last parameter - referred as brightness - gives a diffraction limited microprobe, and combined with the stability of third generation synchrotron radiation facility such as Diamond Light Source, high signal to noise ratio (S/N) spectra. Currently, more than twenty SR facilities around the world provide scientists from a wide range of disciplines with access to IR beamlines for spectromicroscopy and imaging [3], with an emphasis on non-damaging synchrotron-based IR microanalysis for biomedical studies.

There is great interest in using the broad bandwidth and brightness of IR-SR in near-field measurements, which improve on the optical IR microscopy spatial resolution limit of circa λ (based on typical objective numerical aperture NA ~0.5) by using sub-optical wavelength

sized tip structures to detect the local absorption of light. A topic of interest for decades, near-field IR instrumentation has recently developed in applicability and ease of use through the introduction of schemes that are able to measure IR absorption in the near-field with relatively high S/N, either via scattering scanning near-field optical microscopy (s-SNOM) [4, 5], fibre-optic SNOM [6] or via photothermal effects [7, 8]. Photothermal near-field methods detect the absorption of IR radiation through the local temperature rise associated with the relaxation of a sample's excited vibrational modes. This results in local thermal expansion which can be mechanically measured with high sensitivity via an atomic force microscope (AFM) tip in contact with the sample, either exciting the AFM cantilever in an impulsive [7] or resonant [8] manner. Both methods have been shown to give high quality near-field IR spectral images in a variety of analytical contexts [9–11]. The possibility of using scanning tunnelling microscopy (STM) to detect and spectrally image thermal expansion from heated molecular monolayers has also been recently demonstrated [12].

The availability of an increasingly wide range of high power tuneable mid-IR laser sources has played a significant role in the development of near-field IR imaging [4, 5, 8]. In exploiting the broader bandwidth of IR-SR, the key challenge is achieving an adequate S/N from a lower total power than that of laser sources and retaining a high photon flux density at the sample. The improved s-SNOM methods recently reported have circumvented this difficulty and enabled broad bandwidth synchrotron FT-IR to be used for near-field imaging of square ring metasurfaces [13], Au coated SiC [14], semiconductor, biomineral and protein nanostructures [15]. Here we show for the first time that synchrotron FT-IR near-field measurements based on direct photothermal expansion are also possible, with the key advantage of an AFM signal directly proportional to the IR absorbance. This is achieved by applying a resonant cantilever excitation scheme [8] (termed elsewhere as 'Resonance Enhanced AFMIR' or 'RE-AFMIR' [16]) to detect IR-SR induced sample thermal expansion and using interferometry to recover the absorption spectrum. In addition, we revisit a method of measuring photothermal IR spectra using AFM tips for scanning thermal microscopy (SThM) [17]. In this approach, sample heating is measured via changes in electrical resistance of the AFM thermoresistor tip.

2. Signal size and spatial resolution

In a photothermal expansion experiment, the small (~pm) linear thermal expansion of an IR illuminated microsample exerts a force on an in-contact AFM tip and cantilever, exciting the cantilever oscillation modes. In the commonly used laser-bounce AFM configuration for detecting tip motion, the excited cantilever modes modulate the laser deflection angle, resulting in an AC deflection signal on a 4-quadrant photodiode monitoring the laser light [18]. As with any resonant system, the cantilever signal amplitude is a convolution of its response function and the input (driving) function. In this case we may define a cantilever thermal response $\chi(t)$ and light absorption-induced temperature (driving) term $T(t)$ giving rise to signal $S(t)$. Decomposing the cantilever response into a set of sinusoidal terms of angular frequency ω_n damped at rates Γ_n, the convolution takes on the simple form for a set of n driven damped harmonic oscillators:

$$S(t) = (\chi * T)(t) \propto \int_0^t dt' \sum_n \frac{1}{\omega_n} \left(\sin\left(\omega_n(t-t')\right) e^{-\frac{\Gamma_n(t-t')}{2}} \right) T(t') \tag{1}$$

Calculations of $S(t)$ that include explicitly the cantilever modes, thermal expansion and tip deflection signal can be found in the work of Dazzi *et al* [18]. Here, we consider the case where the infrared light is modulated with frequency η, making $T(t)$ periodic. For pulsed temperature excitation at a rate η far from $\omega_n/2\pi$, Eq. (1) describes the 'ring down' signal of impulsive excitation [7]. The response becomes independent of η and dependent only on the

temporal width of each pulse. In the resonant mode [8], where pulsed or sinusoidal excitation is used with $\eta \sim \omega_n /2\pi$, the response is a set of Lorentzians peaked about each ω_n.

It is not surprising that under identical conditions, evaluating Eq. (1) with Gaussian and sinusoidal forms of $T(t)$ results in the resonant mode of operation giving a signal $S(t)$ that is $10^5 - 10^9$ times larger than the impulsive mode, depending on the Gaussian pulse width. The signal to noise ratio in published impulsively measured images is however still very high, this being due to the high laser power delivered to the sample ($\sim 10^9$-10^{10} W m^{-2}). For the case of synchrotron IR excitation, the power delivered to the sample is in the region of 10^5-10^6 W m^{-2} spread over a larger bandwidth. This is the reason for adopting the RE-AFMIR approach in this paper.

For many photothermal experiments, the issue of spatial resolution requires the consideration of thermal diffusion timescales [17]. Vibrationally excited molecules relax on a rapid (<100 ps) timescale, creating a non-equilibrium temperature distribution which then homogenises via thermal diffusion within a given volume $\sim R^3$ on a timescale τ [18]. In the simple case of a homogenous bulk material of thermal diffusivity D_T, the thermal diffusion limited resolution is:

$$R = \sqrt{3\tau D_T} \tag{2}$$

R is the radius of the sphere over which heat created at a central point will have diffused over time τ. In the most common implementations of photothermal near-field IR imaging, pulsed (<10 ns) laser excitation is used. In this limit, thermal diffusion is small and spatial resolution is limited instead by the signal to noise capabilities of the AFM, as well as the AFM cantilever response/tip profile. With both impulsive and resonant modes of excitation, resolutions of 20-100 nm have been reported in literature [12, 19, 20]. In this paper, we use R as a general figure of merit to inform the degree of modulation required for sub-diffraction limited resolution using IR-SR. However, as will be shown experimentally for the samples studied, the actual resolution can be much higher than predicted by this simple metric.

Synchrotron light is intrinsically pulsed, e.g. in a standard user mode, the Diamond Light Source storage ring filling pattern is 900 electron bunches each separated by 2 ns (over 936 buckets available). The single bunch storage ring revolution frequency is ~534 kHz, however the 96% duty cycle used for the experiments reported here means that the IR-SR source can be viewed as essentially continuous. If the IR-SR is modulated by a mechanical chopper, for a given power (denoted P_{abs}, see Appendix) absorbed by the thermal diffusion sphere [Eq. (2)] of thermal conductivity κ, the temperature rise within the sphere is:

$$\Delta T = \frac{P_{abs}}{4\pi R \kappa} \tag{3}$$

Figure 1 shows how the spatial resolution R and a.c. temperature rise ΔT is expected to vary with optical modulation rate, calculated using Eqs. (2)-(4). The thermal/absorption characteristics of a protein sample were used. From these equations, we can see that $\Delta T \propto \eta^{-1}$. A calculation of ΔT within a thermal diffusion volume for a given modulation rate ($\eta = \tau^{-1}$) is shown in Fig. 1 (b) and described in further detail in the appendix. At modulation rates > 100 kHz, we have $R < \lambda/2$ for all wavelengths across the mid-IR part of the spectrum and a temperature modulation in the range of 10 mK.
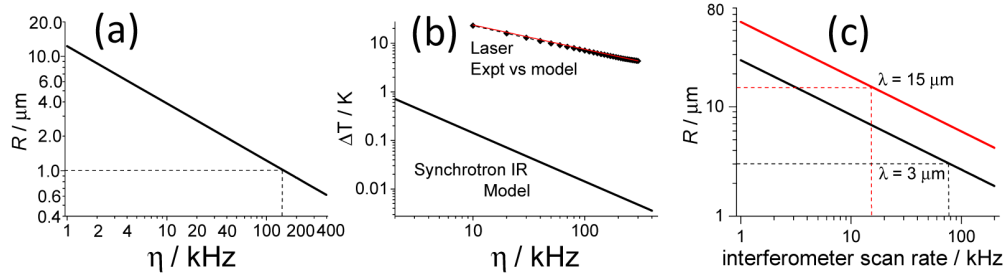
Fig. 1. (a) Calculation of the thermal diffusion radius R as a function of modulation rate η for protein (D_T ~0.05 μm^2 μs^{-1}). (b) The temperature rise within a thermal diffusion sphere of radius R as a function of modulation frequency. The lines are calculations for IR-SR excitation of protein (black line, κ ~0.13 W K^{-1} m^{-1}) and visible laser excitation of dye (red line). The data points are experimental photothermal SThM signal values linearly offset (equivalent to a multiplicative constant accounting for the signal units). (c) Calculation of thermal diffusion radius as a function of IR interferometer scan rate plotted for two wavelengths, 3 and 15 μm. All plots are on a log/log scale. The dashed lines show for several wavelengths the scan rates at which the measurements become sub diffraction limited R < λ.

For FT-IR SThM absorption spectroscopy, detectable modulation can be achieved without a chopper by rapid scanning of the interferometer. Indeed, many early attempts at near-field IR imaging were conducted in this way [17]. This gives a wavelength dependent modulation frequency of $\eta = 2v/\lambda$, where v is the interferometer mirror velocity and λ is the IR wavelength. The interferometer scan rate v is defined as the fringe cycle rate of the HeNe laser (λ = 633 nm) co-aligned in typical interferometers. The IR wavelength modulation rate is therefore $\eta = \eta_{HeNe} \lambda_{HeNe} / \lambda$. It can be seen in Fig. 1(c) that at interferometer scan rates of ~100 kHz, R has reached the diffraction limit ($R<\lambda$) for all mid-IR wavelengths.

3. Experimental

IR-SR is relayed from the source (bending magnet B22 at Diamond Light Source) and into an interferometer (Bruker Vertex 80v, KBr beamsplitter) via several ellipsoidal and toroidal mirrors. Further details regarding MIRIAM beamline B22 can be found in the appendix and reference [21]. Upon exiting the interferometer, the IR light was focussed through a high speed chopper (Scitec instruments, modified with two optoswitches, 445 slot disc) and re-collimated [Fig. 2(a)]. The chopper blade slot width was ~0.3mm with a 50% duty cycle. A maximum chopping rate of 150 kHz (20 krpm) was achieved, limited only by the bandwidth of the on-board counting electronics. The chopper was operated in the same vacuum as the interferometer (~1 mbar) and mounted in a separate enclosure on a steel block and plate. The measured acoustic noise was lower than other sources in the lab up to 150 kHz. The frequency of the chopper was stabilised in closed-loop by a Delta Tau Geobrick control system to a standard deviation phase jitter of ~3°.
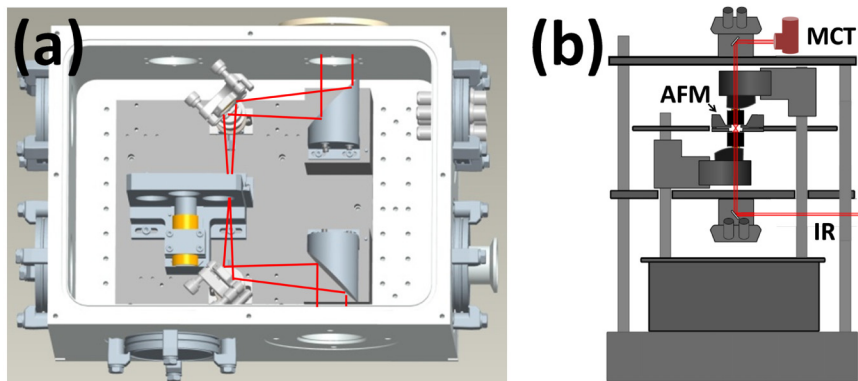
Fig. 2. (a) Chopper optics and vacuum box (optical path shown in red). (b) Optics frame for AFM.

After exiting the chopper box through a KBr window, the IR-SR beam was directed into a dual infinity corrected microscope, Fig. 2(b), and focussed onto an AFM tip using one of several 15x Cassegrain objectives (Spectratech, NA = 0.52, Agilent, NA = 0.62). The 12.5 mm back aperture (pupil) of the Cassegrains were estimated to be filled at λ = 15 μm. For aiding alignment, the beam was refocused onto an MCT detector mounted above the AFM (Fig. 2(b)). A 635 nm diode laser and a 6 μm quantum cascade laser (QCL, Daylight Solutions) were used for offline optimisation of the setup. A Nanonics MV1000 AFM mounted on a vibration isolation stage (Minus K) was positioned in the focus of the Cassegrain objective. The photothermal expansion component of the deflection signal was recovered using lock-in detection (Signal Recovery). The entire microscope was enclosed in an acoustically shielded box. Polystyrene (PS) films and ridge samples were prepared by drop-casting PS dissolved in toluene onto CaF_2. Cyanoacrylate ridges were prepared similarly using commercial glue (Loctite). Mammalian cell (DLD1) samples were prepared on CaF_2 following the procedures of reference [22].

4. Results I. Offline assessment of spatial resolution and tip effects

The spatial resolution achievable using RE-AFMIR for a 40 ns pulsed QCL source has been previously discussed, with 20-50 nm demonstrated for thin polymer films [8, 19]. In general, how the temperature distribution induced by the IR excitation and changes in the resonance frequency both convolve with sample topography in RE-AFMIR images remain an open question. Here we address these issues in the context of the IR-SR experimental data presented in the next section.

As remarked earlier, the IR-SR beam used for the studies in this paper was effectively continuous. Mechanical chopping of the beam imposed a triangular temporal modulation on the intensity. Unlike the instantaneous short-pulse excitation of other photothermal AFMIR work [8, 19], the triangular modulation gives rise to a more gradual temperature rise and cooling, allowing thermal diffusion effects to play a greater role. To explore the impact of thermal diffusion on spatial resolution, we made offline RE-AFMIR measurements on similar samples to those examined with IR-SR (presented in the next section), using the same microscope and vacuum mechanical chopper. A QCL running in CW mode was used as the IR source and chopped mechanically at a rate of around 68 kHz to match the resonance frequency of the Au coated Silicon cantilever used (BudgetSensors).
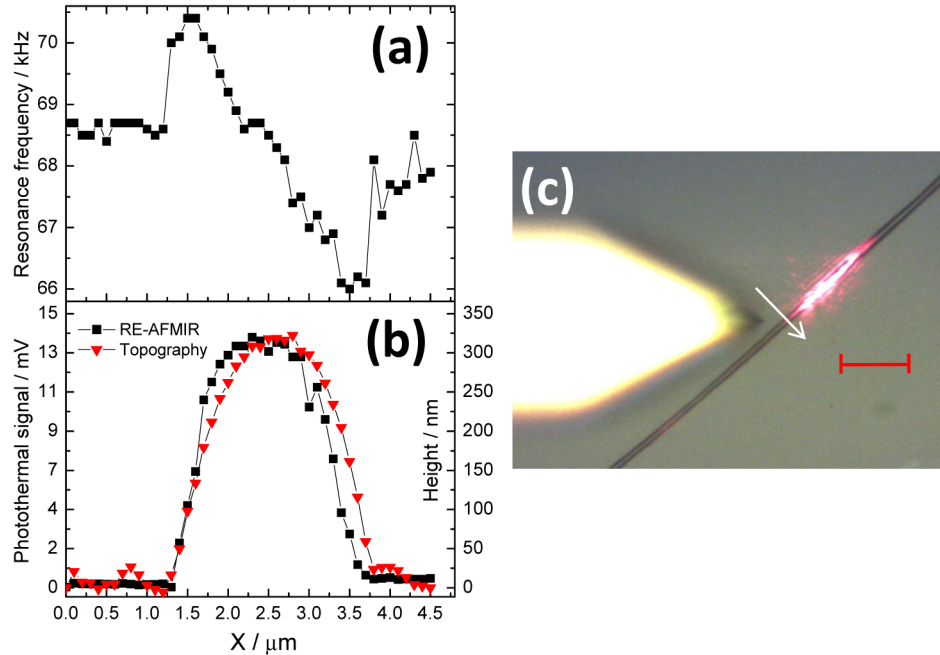
Fig. 3. Plot of cantilever resonance frequency (a), RE-AFMIR signal and topography (b) against position across a cyanoacrylate ridge (shown in (c) alongside AFM cantilever, scale bar 15 μm, white arrow showing scan direction). The RE-AFMIR signal was recorded using a mechanically modulated CW QCL at 1650 cm^{-1}. In (b), the thermal signal (black square) traces the topographic signal (red triangle) to within ~250-500 nm. The signals were recorded at 100nm intervals.

A circa 2 μm wide, 200–400 nm high, ridge of cyanoacrylate deposited onto a CaF$_2$ substrate was examined. A strong 1650 cm^{-1} absorption band of the sample was excited by the QCL. Rather than using a continuous AFM scan mode, the AFM tip was stepped and halted for averaging, as it was observed that the contact resonance frequency varied by ~4 kHz as a function of the slope on the ridge. The laser modulation frequency was therefore optimised at each point to maximise the signal. Failure to do so resulted in a photothermal width profile narrower than the topography due to the attenuation of the photothermal signal at the edges. Figure 3(a) shows a plot of optimised resonance frequency across the ridge. The clear derivative shape points to a systematic variation of the contact spring constant with slope on either side of the tip. We note that even off the ridge on the flat substrate, optimisation of the small but non negligible background was readily achieved, with Fig. 3(a) showing that the frequency giving maximum signal off the ridge is close to the frequency on the maxima (flat part) of the ridge. In Fig. 3(b), the photothermal signal traces the topography change across the ridge to within 250 nm. There is still a slight influence from the changing resonance frequency, with the signal higher on the left hand side of the slope compared with the right hand side. The distance over which both the photothermal and height signals change from 10% to 90% is 500 nm. This demonstrates that at worst the spatial resolution is λ/12, which is clearly sub-diffraction limited. It is interesting to note that this resolution is far better than the 1.5 μm resolution predicted by the simple thermal diffusion arguments of Eq. (2), because the substrate (which has a much lower thermal expansion coefficient and much higher thermal conductivity), produces practically no RE-AFMIR signals.

We examined the validity of Eq. (3) by measuring the thermal response of a Pt thermoresistance SThM AFM tip over a range of modulation frequencies (the SThM tip was used because its response is independent of modulation frequency). The tip, in contact with an

optically thick dye film was illuminated with a sinusoidally modulated laser diode at frequencies up to 120 kHz. As predicted by Eq. (3), in the log/log plot of Fig. 1(b), the SThM signal voltage (proportional to temperature) was indeed observed to be a linear function of modulation rate.
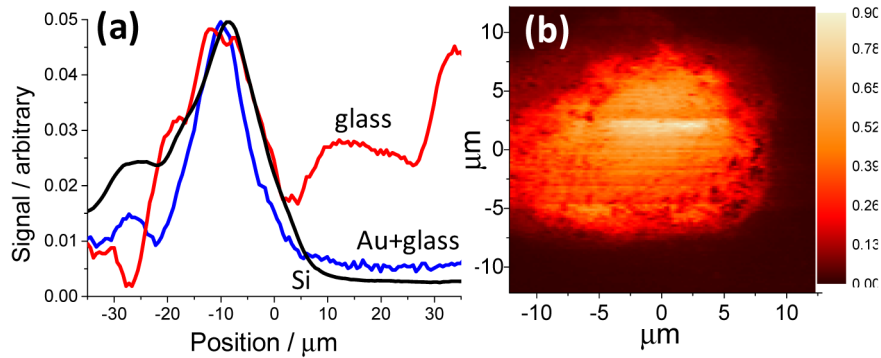

Fig. 4. Tip heating effects. RE-AFMIR signals from different cantilevers on a fixed cell (mammalian DLD1 on CaF_2). A pulsed QCL with $\lambda = 6$ μm (amide I absorption) was used to illuminate the cell. (a) Thermal expansion signal scans of same cell taken with glass cantilever (red, resonant frequency 98 kHz), gold coated glass cantilever (blue, resonant frequency 107 kHz) and silicon cantilever (black, resonant frequency 63 kHz). (b) Photothermal expansion image of DLD1 cell measured using silicon cantilever (resonant frequency 150 kHz).

The dependence of photothermal signals on tip heating and on the Q factor of the tips was explored. Tip heating (through optical absorption) is known to give strong background signals in photothermal experiments [20] and the Q factor of the tips affects the size of the RE-AFMIR signal. To assess these effects, pulled glass fibre tips (bare and gold coated, Nanonics), Si contact mode AFM tips (BudgetSensors and ATEC) and pulled gold coated fibre SThM tips (Nanonics) were tested using IR (QCL) light at 6 μm to image fixed DLD1 cells on CaF_2. In all cases, a tip heating background signal was observed. As expected, for resonant photothermal expansion, under $\lambda = 6$ μm illumination, due to its strong absorption of light, the background signal from glass fibre contact mode tips was observed to be ~10 times larger than that of Si, which is transparent at 6 μm. An 80 nm thick Au coating on the glass fibre (to reflect the IR light) reduced the background to just twice that of Si. Figure 4 illustrates these effects for the imaging of a fixed cell, with the artefact most severe for the case of bare glass tips. For this case, the peak signal from the fixed cell is comparable in size to the background signal. For SThM tips the background heating signal was found to be several times larger than the fixed cell heating signals (not shown).

In Fig. 4(a), the S/N of the data from the stiffer and lighter Si cantilever is clearly superior to the glass fibre cantilever data, due to its higher Q contact resonance. Therefore, despite the glass tips being much more robust and easier use, Si cantilevers are much more suitable for detecting weak signals in IR-SR experiments.

4. Results II. Resonance enhanced AFM-IR spectra using infrared synchrotron radiation

In this section we demonstrate for the first time the acquisition of broadband RE-AFM FT-IR spectra using IR-SR under conditions proven in the previous section to be sub-diffraction limited. Figure 5(a) shows an IR-SR photothermal expansion spectrum of a thin PS film deposited on CaF_2. An Au coated glass fibre cantilever, [Fig. 4(b)], was used for these measurements. The peak optical density of the film where the AFM measurements were made was around 0.5 (2926 cm^{-1}, C–H stretch), measured using far-field IR microscopy. This corresponds to a film thickness of roughly 500nm. The incoming IR light was modulated at the 106 kHz resonance frequency of the in-contact tip; Fig. 5(d). During acquisition, the total

amplitude of the thermal expansion signal from the beam bounce photodiode was 100 ± 10 μV, as measured through a lock-in amplifier. Under these conditions, using a lock-in time constant of 500 μs, an interferometer scan rate of 1.6 kHz and a resolution of 8 cm^{-1}, interferograms directly transformable into heating spectra could be recorded. The interferometer scan rate of was set to give a signal modulation timescale *longer* than the timescale required for the lock-in detection. Here, 1.6 kHz, which corresponds to a 3−10 ms FTIR signal modulation timescale over the λ = 3−10 μm wavelength range recorded. This is a few times longer than the lock-in detection time constant of 500 μs. No background tip heating signal is observable in the data.

Figure 5(a) shows that the measurement of sub-diffraction limited near-field tip-resonant thermal expansion IR absorption is feasible when using IR-SR as an excitation source and an interferometer for analysing the response spectrum. In comparison to standard IR spectromicroscopy on the same sample shown in Fig. 5(c), it is worth noting that all major spectral features characteristic of the polymeric film are retained in the SR-IR AFM signal. At the 106 kHz modulation rate, the thermal diffusion-limited spatial resolution was in the region of 1 μm as described in Fig. 1(a). As shown earlier in Fig. 3, the actual resolution over a ridge of sample is likely to be better than this.
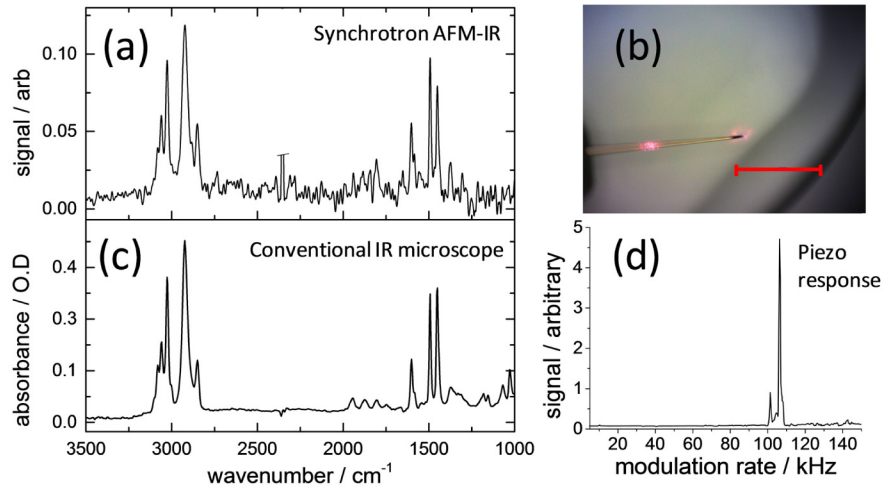

Fig. 5. (a) IR-SR photothermal expansion spectrum of a PS film recorded using an Au coated glass fibre cantilever with a resonant frequency of 106 kHz. (b) Image of the cantilever, with the SR beam focussed under the tip, during the measurement (scale bar is 400 μm). (c) IR spectrum of the same region of the PS film recorded using conventional IR microscopy. (d) Tip response spectrum of the Au coated glass fibre cantilever used.
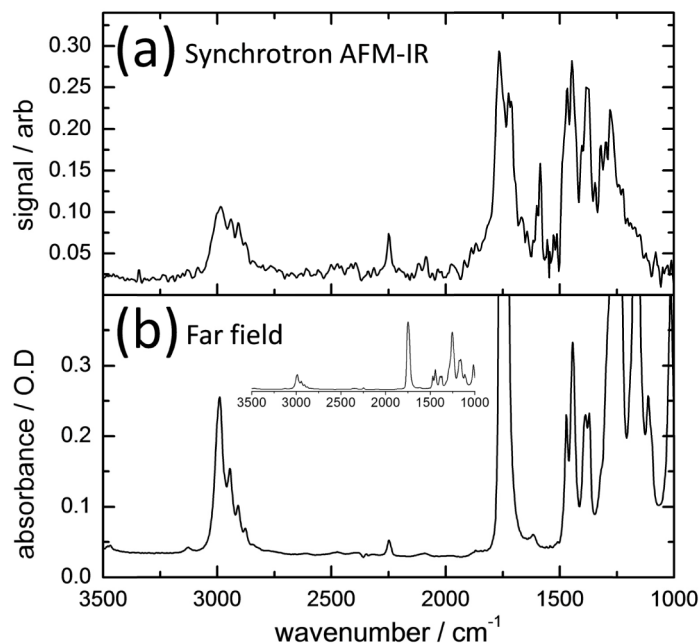
Fig. 6. Comparison of (a) near and (b) far-field spectra for a cyanoacrylate microsample. The near-field spectrum was taken with an Au coated Si tip in 15 minutes. The inset in (b) shows the far-field spectrum full-scale.

Figure 6 (a) shows a near-field spectrum for a microsample of cyanoacrylate on CaF_2, where the data was acquired using an Au coated Si cantilever (BudgetSensors**)** at a resonance frequency of 76 kHz. For the Fig. 6 measurements, a slightly modified optical setup using a higher numerical aperture objective (Agilent, NA = 0.62) in order to increase the effective flux delivered to the tip. These improvements, coupled with the use of the higher Q Si cantilever resulted in 3 to 10 times increase in photothermal IR signals observed compared with the setup used to record Fig. 5. For Fig. 5(a), the acquisition time was 150 minutes. The near-field spectrum in Fig. 6(a) was taken in 15 minutes, demonstrating that imaging with SR-IR RE-AFMIR is feasible. Comparison with a representative far field IR spectrum of cyanoacrylate [Fig. 6 (b)] shows that all key vibrational features, such as the 2225 cm^{-1} band associated to a CN mode, the 1750 cm^{-1} (CO stretch) and 1615 cm^{-1} (CC stretching), are correspondingly present in the near-field IR spectrum. Unlike Fig. 5, relative band intensity correlation between Fig. 6 (a) and (b) is not expected, as there are clear saturation effects on the strongest IR absorption bands e.g. the CO stretching mode.

The acquisition of higher signal to noise data is anticipated in future by the following improvements; increased optical delivery efficiency, higher Q cantilevers, developing a more robust means of finding and optimising the RE-AFMIR signal and exploring the dependence of the resonance frequency and signal on the AFM feedback controls. It was found that in order to reduce feedback noise in the raw AFM photodiode signal, the proportional gain needed to be reduced substantially, which in turn often affected the stability of the cantilever when landing on and in contact with the sample. To remedy this and also to account for sample induced variation in contact resonance frequency, active control and checking for cantilever resonance frequency shifts and proportional gain would be desirable.

5. Results III. Photothermal SThM absorption spectroscopy using infrared synchrotron radiation

The high efficiency Cassegrain optics employed in this paper afforded an opportunity to re-examine the SThM method of recording IR-SR spectra. The important advantage compared to RE-AFMIR is the relaxation of the constraint to modulate the beam at the cantilever resonance frequency. SThM measurements to date have however not achieved sub-diffraction limited resolution, with previous IR-SR work [17] reporting significantly lower flux delivered to the tip than was achieved in this study. For the IR-SR SThM measurements reported here, the large tip heating background signal was relatively easy to identify and align in the synchrotron focus. The SThM probes used (Nanonics Pt thermoresistive probes, 100nm Au overcoat) were very fragile, their finite in-use lifetime imposing a large practical constraint on experiments. The SThM probe failure rate was a function of sample flatness, current delivered across the probe, scanning mode and feedback settings. Larger currents gave higher signal to noise, however they also increased the likelihood of probe failure. AFM feedback optimisation is always required when using a new tip, however for the SThM probes, suboptimal feedback would cause instant tip failure. Once scanning reliably, tips could be used with care on several samples (hours of scanning) before failure. Figure 7(a) shows the tip in the vicinity of fixed DLD1 cells on CaF_2. For these experiments, interferograms were recorded directly from a Wheatstone bridge balance voltage output proportional to the tip electrical resistance [17]. Shown in Fig. 7(b) are spectra transformed from interferograms recorded at different FT-IR scan speeds, with the SThM probe in direct contact with a fixed cell. The amide I and II absorption bands of the single DLD1 cell are present in this data, but better observed after the strong tip heating background is eliminated by subtracting bare CaF_2 signal, as is shown for an interferometer scan rate of 40 kHz in Fig. 7(c). Figure 7(d) shows for comparison a spectrum of a DLD1 cell recorded using a conventional mapping IR-SR microscope at 15μm resolution.

The total acquisition time for the data in Fig. 7(c) was ~40 minutes. The attainment of spectral data from a fixed cell at 40 kHz interferometer scan speed is a clear step forward compared with past attempts of SThM probing of synchrotron based IR absorption spectroscopy [17]. In terms of resolution, the 40 kHz interferometer scan rate gives IR modulation rates of 2.5−8.5 kHz over the 3−10 μm wavelength range probed, corresponding to thermal diffusion length scales (R) that are smaller than the far-field diffraction limited spatial resolution limit ~λ at wavelengths >6 μm. Measurements with the 150 kHz chopper would provide the necessary modulation to make the resolution at all wavelengths close to 1 μm, but reduce signal sizes by more than an order of magnitude.
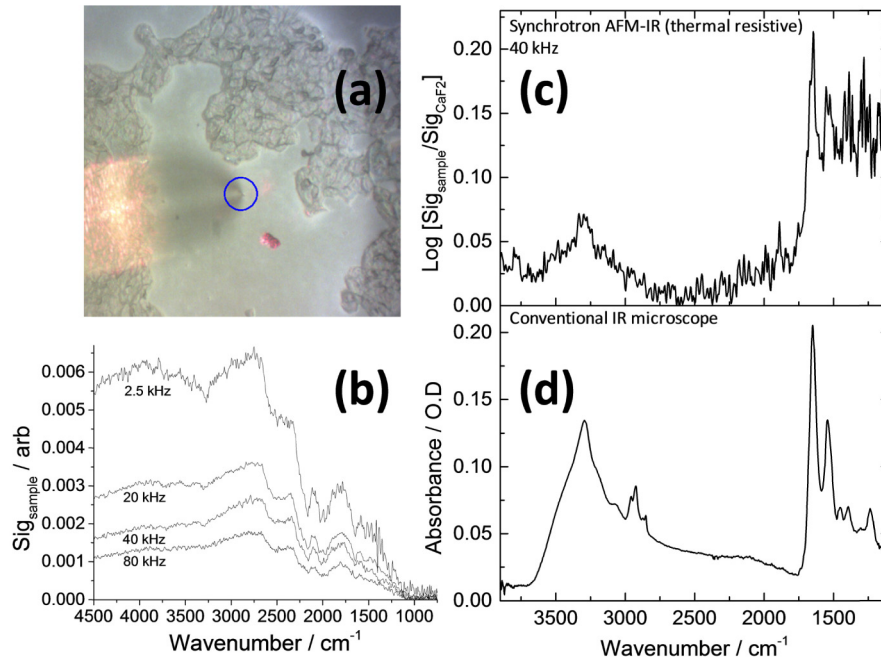
Fig. 7. Synchrotron IR photothermal SThM spectra of fixed DLD1 cells on CaF$_2$. (a) A Nanonics SThM probe with 100 nm gold overcoat in the vicinity of DLD1 cells. (b) Photothermal IR spectra of the SThM probe in contact with DLD1 cells for different interferometer scan rates. (c) A background subtracted DLD1 photothermal absorption spectrum obtained by logarithmic subtraction of spectra on the cells and on the bare window. (d) An infrared spectrum of a fixed cell measured using a conventional single point mapping microscope at 15 μm resolution.

6. Conclusions

In this paper we have shown for the first time measurements of RE-AFMIR spectra using broadband IR-SR and interferometric Fourier transform acquisition. FT-IR absorption spectra were recorded across a continuous 3−10 μm bandwidth from films and micro ridges of polystyrene and cyanoacrylate. As a very first report of IR-SR RE-AFMIR spectra, mapping was not performed, however under very similar sample and experimental conditions, the spatial resolution of the method was tested using an offline QCL and confirmed as better than λ/12 at 6 μm. Acquisition times of 15 minutes per near-field IR-SR spectrum were experimentally demonstrated. Although acceptable for spectromicroscopy and line mapping, the collection of an images requires hundreds or more points. A factor of ten reduction in acquisition time is therefore required for acceptable IR imaging timescales. This reduction in this time is expected through improvements in delivery optics, increase in AFM probe Q factors, signal recovery and stabilisation of the contact mode resonance frequency, opening up the possibility for IR nanoimaging using this new technique.

For comparison, we also revisited the photothermal SThM method using IR-SR excitation. Although the IR spectra obtained from fixed cells demonstrates higher signal to noise ratio under conditions closer to diffraction limited resolution than any previous published studies, based on the sample absorption coefficients and the optical modulation rates in each case, it can be concluded that the RE-AFMIR approach has a significant advantage in terms of S/N, therefore allowing spectral acquisitions at a higher spatial resolution.

7.1. Appendix 1. The bending magnet IR source at Diamond.

A storage ring bending magnet emits synchrotron radiation into an angular range set by the wavelength of light and the collection optics of the beamline. On the MIRIAM beamline at Diamond, light is collected into an angular range of 50 mrad (horizontal) x 30 mrad (vertical). The synchrotron radiation field pattern contains a central horizontal node about which a slotted first mirror is used after the bending magnet to remove the X-rays, which are less divergent than the IR light. A total of ~2 mW over a 2 - 25 μm bandwidth is delivered to the beamline end window from a 300 mA circulating current.

An important parameter for achieving maximum intensity at an optical microscope focus is the angular range over which the beam can be considered as coming from a point source (the natural opening angle θ_{nat} [23]). θ_{nat} increases with wavelength. For the experiments reported here, the delivery optics were arranged such that the back aperture of the Cassegrain objective used for focussing light on the sample was estimated as being optimally illuminated with an SR-IR source opening angle of 21 mrad, corresponding to a wavelength of 15 μm and roughly one third of the total power available. For wavelengths above/below this amount, the objective is over/under filled, reducing the focussed power density for these wavelengths. After passing through an interferometer (50% loss), we estimate in the reduced 3-12 μm wavelength range that the total focussed power was around 25-50 μW.

7.2. Appendix 2. Temperature rise of a sample in focussed synchrotron IR light.

An estimate of ΔT within a thermal diffusion volume $\sim R^3$ of a protein film illuminated by synchrotron IR at a modulation rate η [Fig. 1(b)] is described here. The total focussed power for the experiments reported was ~25-50 μW, delivered to a ~20 μm spot fwhm. The (known) incident photon flux per unit bandwidth for the synchrotron radiation is expressed as $E_{inc}(\lambda)$. Combined with complex refractive index data $n(\lambda)+ik(\lambda)$ measured from a protein film (BSA), we estimate P_{abs} by calculating [18]:

$$P_{abs} = \int_{\lambda=3\,\mu m}^{\lambda=12.5\,\mu m} d\lambda \frac{2\pi}{\lambda} c\epsilon_0 \frac{9n(\lambda)k(\lambda)}{(n(\lambda)+2)^2} |E_{inc}(\lambda)|^2 \frac{4\pi R^3}{3} \tag{4}$$

Equation (4) is valid under the dipole approximation and is only reliable when none of the dimensions of the protein 'film' are similar to the wavelength of light λ. Equations (2) and 3 can then be considered as describing the a.c. temperature amplitude in a given region of the protein film once the system has reached a steady state under modulated IR illumination. Interface thermal effects are not accounted for.

In Fig. 1(b) we estimate the temperature rise in an optically dense sample for a visible laser based thermal resonance experiment. Based on total power P_{tot} of 1 mW 100% absorbed in a ~10 μm spot, we approximate the power absorbed as $P_{abs} \approx P_{tot} A_{thermal} / A_{tot}$, where A_{tot} is the area of the laser focus and $A_{thermal}$ is the thermal diffusion area. This approximation is applicable when the $1/e^2$ absorption length $l << R$ and is a reasonable assumption for the case of the strong dye absorber used for the measurement in Fig. 1(b).

Acknowledgments